Semiconductors, 2024, Vol. 58, No. 12

Electron and hole mobility in carbon hybrid structures

© *O.E. Glukhova*[1,2], *M.M. Slepchenkov*[1], *A.A. Petrunin*[1,¶]

[1] Saratov National Research State University,
410012 Saratov, Russia
[2] Sechenov First Moscow State Medical University,
119991 Moscow, Russia
[¶] E-mail: sacha.petrynin@gmail.com

Received July 10, 2024
Revised October 21, 2024
Accepted December 23, 2024

Within the framework of density functional theory, we conducted a study of the influence of topological features on the mobility of electrons and holes in hybrid graphene-nanotube structures, where the vertically oriented graphene nanoribbon is covalently attached to the lateral surface of the single-walled carbon nanotubes. Topological features are understood as the diameter of the nanotube and the width of the nanoribbon. It has been established that increasing the diameter of the nanotube from 6.26 to 12.52 Å leads to an increase in electron mobility in hybrid structures by more than 50 times. With an increase in the width of the nanoribbon from 9.81 to 22.17 Å and a fixed diameter of the nanotube (12.52 Å), the electron mobility also increases, but only by ~ 1.5 times.

Keywords: charge carrier mobility, effective mass, deformation potential, graphene-nanotube structures.

DOI: 10.61011/SC.2024.12.60386.6872

1. Introduction

Carbon nanotubes (CNT), graphene and graphene nanoribbons (GNR) have been widely used in various fields of electronics over the last decades due to their unique properties, such as mechanical strength and chemical stability, which ensure long-term device operation and high electrical conductivity and emission current density [1–6]. One of the promising applications of CNTs and graphene is autoemission electronics. In [7], it is shown that a graphene-based bulk field emitter provides stable electron emission for 60 h at a current of 3.3 mA (current density of 209.78 mA/cm^2). Another paper [8] presents an X-ray tube with a CNT-based field emission cathode, which has an extremely high current density of 152 A/cm^2 (corresponding to a current of 106.4 mA) and a long lifetime with stable operation over 100 000 shots. At the same time, CNT-based cold cathodes are low-voltage and characterized by a small electron beam diameter [9]. The use of CNTs and graphene in creating transistor devices is just as promising. Thus, [10] proposed a field-effect transistor based on a hybrid material „graphene + MoS$_2$" and showed that the mobility of charge carriers in it is ~ 10 times ($\sim 100\,\mathrm{cm}^2/(\mathrm{V}^{-1}\cdot\mathrm{s}^{-1})$) higher compared to the mobility of carriers in a molybdenum sulfide monolayer MoS$_2$. CNT-based field-effect transistors with MIS structure are used in the formation of ultra-low-power static memory bit cells to be later used in radiation-hazardous low-orbit environments where power supply resources are limited [11].

The successful application of CNTs and graphene in various electronics applications has laid the groundwork for the development of CNT-graphene hybrid materials characterized by improved properties compared to their structural components [12–21]. In particular, in [12] it is shown that the CNT-graphene hybrid films show a field enhancement factor of 5750 and an emission current of 80 mA (current density of 160 mA/cm^2), which exceeds that of individual single-walled CNTs (SWCNTs) and graphene films. Seamless CNT-graphene hybrid structures obtained in [13] are characterized by a current density of 236 mA/cm^2 and a field enhancement factor ~ 41315 at an inclusion field value of 0.45 V/μm. It has been experimentally found that the microcavities of nanostructured carbon consisting of SWCNT and graphene fragments provide a steady current of ~ 2 mA (current density ~ 112 mA/cm^2) at the applied field < 2 V/μm [14].

One of the promising applications of CNT-graphene hybrid nanomaterial is flexible and stretchable electrodes. The hybrid structure combining CNTs of metallic conductivity type and graphene retains high electrical conductivity under significant deformation [15–17]. The CNT-graphene hybrid films [18] have lower surface resistivity ($420\,\Omega\cdot\Box^{-1}$) than those based on graphene alone ($2.15\,\mathrm{k}\Omega\cdot\Box^{-1}$). The improved electrical conductive properties of hybrid graphene-nanotube nanomaterials are attributed to the low graphene-CNT contact resistance due to $\pi-\pi$-interactions between graphene and the nanotube. Field-effect transistors based on all-carbon structures have a number of unique advantages over field-effect transistors based on other nanomaterials. For example, a paper [19] discusses the development of transistors based on monolayer graphene and CNTs on flexible substrates. The authors found that the contact resistance of CNT-graphene is 100 times lower than that of CNT-gold, while a 20-fold increase in carrier mobility was observed in these structures compared to the CNT-gold material (to $81\,\mathrm{cm}^2/(\mathrm{V}^{-1}\cdot\mathrm{s}^{-1})$), and the change in resistance of CNT-graphene films when stretched by 50% was 36%.

To determine the underlying mechanism of changes in the electrical conductive and emission characteristics of CNT-graphene hybrid films compared to individual nanotube and graphene, studies should be carried out using *ab initio* methods, which allow us to take into account the quantum nature of the emerging physical phenomena and effects. An important aim is to identify the topological features of graphene and CNTs in the hybrid material, which have the greatest influence on the magnitude of mobility. Such studies have been carried out for a hybrid nanostructure based on CNT (8,0) and a graphene fragment covalently attached to the side surface of the nanotube [20,21]. In [21], numerical estimates of the electron mobility ($2250\,\mathrm{cm}^2/(\mathrm{V}^{-1}\cdot\mathrm{s}^{-1})$) are obtained for this structure. However, the authors do not explain how these results were obtained, which does not allow for their physical interpretation. No other work has been found where the mobility of charge carriers in hybrid graphene-nanotube structures has been numerically evaluated.

The purpose of this work is to identify the regularities of charge carrier mobility in hybrid SWCNT/GN structures depending on the topological parameters of SWCNTs and GNTs included in these structures. The $1D$-hybrid structure formed by a single-wall tube and a graphene nanoribbon attached covalently to the side surface of the tube was chosen as the object of study. The diameter of the tubes ranges from 6.264 to 12.529 Å, the width of GH ranges from 9.81 to 22.17 Å.

2. Research methods

The hybrid nanostructures were simulated using density functional theory (DFT) within the generalized gradient approximation (GGA) as formulated by Perdew-Burke-Ernzerhof in the SIESTA (version 4.1.5) [22] software package. Pseudopotentials with a basis set of DZP (double ξ plus polarization) [23] type were used to estimate the interaction energy of graphene sheets and carbon tubes. In finding the equilibrium atomic configuration of the supercells, integration in inverse space over the first Brillouin zone was performed by the Monkhorst–Pack method with grid partitioning into 16 points along the translation axis. A more accurate partitioning of 200 points was used in the calculation of the band structure. The cutoff for the kinetic energy was 600 P (Rydberg) Ry, and the convergence in force magnitude did not exceed 0.001 eV/Å.

To calculate the charge carrier mobility, we used the formula obtained for $1D$-structures [24] within the framework of the Bardeen and Shockley [25] deformation potential theory developed to estimate the charge carrier mobility of crystals:

$$\mu_\beta^{1D} = \frac{e\hbar^2 C_{1D}^{\beta}}{(2\pi k_\mathrm{B} T)^{1/2}\, m^{*3/2} E_\mathrm{B}^2}, \tag{1}$$

where $\hbar$ — reduced Planck constant, k_B — Boltzmann constant, T — temperature, C_{1D}^{β} — elasticity constant, E^β — deformation potential, m^* — effective mass of charge carriers (holes or electrons).

The elasticity constant C_{1D}^{β} characterizes the interaction of electrons with phonons and is determined during stretching and compression of the supercell of the nanostructure according to the formula

$$C_{1D}^{\beta} = \frac{1}{l_0}\,\frac{\partial^2 E}{\partial\left(\partial l/l_0\right)^2}, \tag{2}$$

where E — total energy, l_0 — translation vector of $1D$-structure. Value $\partial l/l_0$ specifies the stretching (in 1.0025 and 1.005 times) and compression (in 0.995 and 0.9975 times) of the supercell of the structure along the translation vector.

The deformation potential E^β is given as follows:

$$E^\beta = \frac{\Delta V_i}{\Delta l/l_0}, \tag{3}$$

where ΔV_i — the energy change of the i-th subband when the $\Delta l/l_0$ supercell is stretched and compressed along the β direction.

The effective mass of charge carriers m^* is defined as

$$m^* = \frac{\hbar^2}{(d^2E)/(dk^2)}. \tag{4}$$

In order to calculate the $(d^2E)/(dk^2)$, the lower subband of the conduction band (conduction band floor) and the upper subband of the valence band (valence band top) are extracted from the calculated band structure. Parabolic interpolation is applied to each of the two selected subbands, which is a necessary condition for the calculation of isotropic charge carrier transport [24,25]. The second derivative $(d^2E)/(dk^2)$ is calculated near the point Γ in the band structure, with the effective electron mass m_e^* calculated over the lower subband of the conduction band and the effective hole mass m_h^* — over the upper subband of the valence band.

The mobility of charge carriers in hybrid SWCNT/GNR structures was calculated according to the following algorithm:

– obtaining the equilibrium atomistic configuration of the hybrid SWCNT/GNR structure;

– calculation of the effective mass of charge carriers m^* of the hybrid SWCNT/GNR structure;

– stretching and compression of the supercell of the SWCNT/GNR hybrid structure. For each supercell of the investigated structure, 4 different cases of deformation along the direction of the translation vector were considered: compression by 0.995 and 0.9975 times, stretching by 1.0025 and 1.005 times;

– calculation of the total energy of each of the considered supercells of the SWCNT/GNR hybrid structure. Calculation of the elasticity constant C_{1D}^{β};

– construction of the band structure for each of the considered supercells of the SWCNT/GNR hybrid structure and

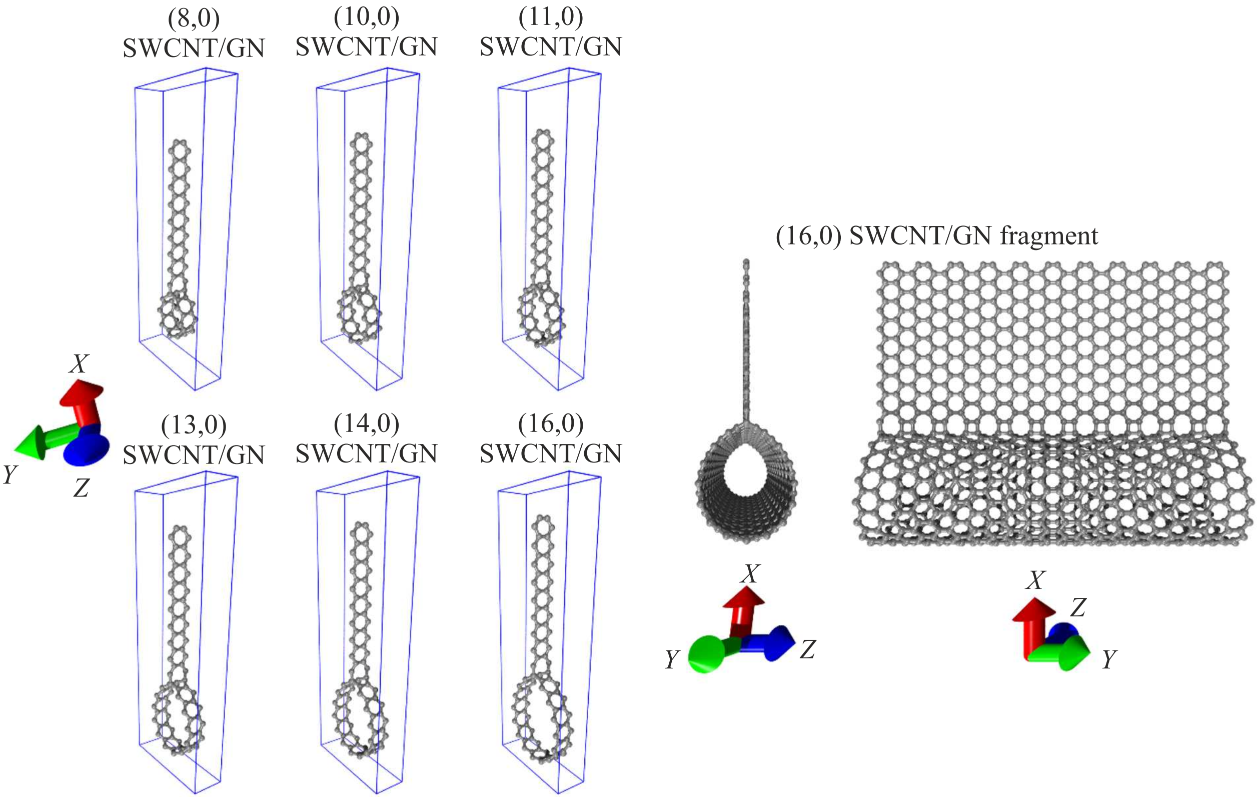

Figure 1. Equilibrium supercell configurations of hybrid CNT/GNR structures with nanotubes of different chirality and nanoribbons of fixed width (22.17 Å), as well as an extended fragment of a graphene-nanotube 1*D*-structure consisting of several (16,0) CNT/GN supercells. (A color version of the figure is provided in the online version of the paper).

determination of the valence band top and the bottom of the conduction band. Calculation of deformation potential E^{β};

– calculation of charge carrier mobility μ_{β}^{1D} of the SWCNT/GNR hybrid structure using the known values of m^*, C_{1D}^{β}, E^{β}.

3. Results

3.1. Building of 1*D*supercells of graphene-CNT structures

CNTs with chirality indices (8.0), (10.0), (11.0), (13.0), (14.0), and (16.0) of semiconductor conduction type were used to construct supercells of hybrid SWCNT/GNR structures. The „zigzag" tubes were chosen because of the small number of atoms in the composition of their supercells compared to chiral tubes. For example, the supercell (8,4) of SWCNTs contains 112 atoms, while the supercell of the largest nanotube (16,0) among those investigated in this work contains only 64 atoms. During supercell construction, the „chair" type GNRs were attached to the SWCNT wall by covalent bonds, forming an octagonal compound. Figure 1 shows the equilibrium atomic configurations of the constructed supercells of SWCNT/GNR hybrid structures with fixed-width (22.17 Å) nanoribbons and an extended fragment of the structure consisting of several (16.0) SWCNT/GNR supercells. It can be clearly seen that during the formation of energy-stable covalent bonding between GNR and SWCNTs, the nanotube was strongly elongated in the X axis direction, acquiring a near elliptical geometric shape instead of the cylindrical shape of the nondeformed nanotube. We did not passivate the edges of the nanoribbon with hydrogen atoms in the non-periodic direction (axis X), because the carbon atoms in this direction form an edge in the shape of „chair" and, according to the data of [26], are characterized by *sp*-hybridization due to strong dimerization, so they do not contain unsaturated bonds.

The translation vector of the SWCNT/GNR hybrid structures is directed along the Y axis (green axis in the figure). The length of this vector was 4.294, 4.293, 4.293, 4.292, 4.291, 4.290 Å for the hybrid structures with SWNTs (8,0), (10,0), (11,0), (13,0), (14,0), and (16,0), respectively. As can be observed, the translation vector of the hybrid SWCNT/GNR structure decreases with the increase of the tube diameter, which, as will be shown later, is related to the increase of the elasticity constant. Thus, the number of atoms for the graphene-nanotube structures with SWCNTs (8.0), (10.0), (11.0), (13.0), (14.0), and (16.0) were 68, 76, 80, 88, 92, 100, respectively.

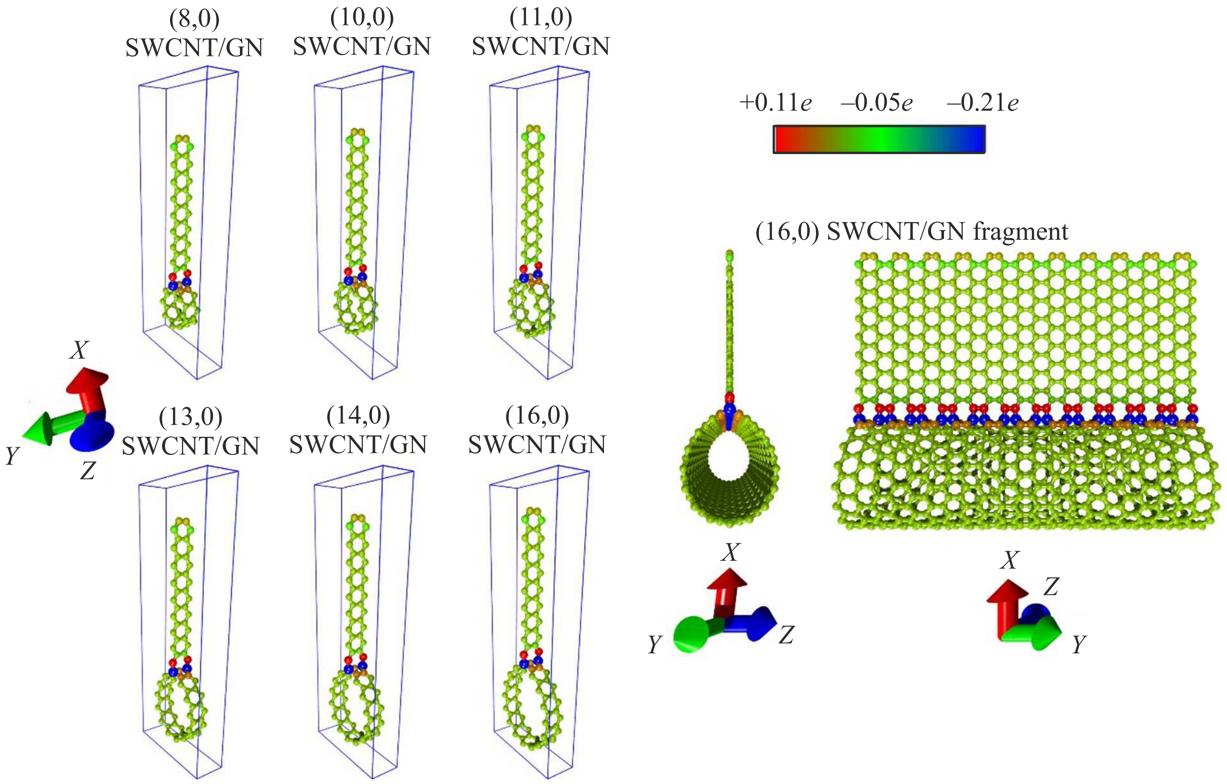

Figure 2. Mulliken distribution of electron charge density over the supercell atoms of SWCNT/GNR hybrid structures with nanotubes of different chirality.

Table 1. Values of the effective mass of electrons m_e^* and holes m_h^* in units of electron mass m_0, elasticity constant C_{1D}^{β}, deformation potential of electrons E_e^{β} and holes E_h^{β}, mobility of electrons μ_e^* and holes μ_h^* in the hybrid structures of SWCNT GNR and their structural components.

	m_e^*, $0.01m_0$	m_h^*, $0.01m_0$	$C_{1D}^{\beta} \cdot 10^{11}$, eV/cm	E_e^{β}, eV	E_h^{β}, eV	μ_e^*, $\mathrm{m^2/(V \cdot s)}$	μ_h^*, $\mathrm{m^2/(V \cdot s)}$
(8,0) SWCNT/GNR	3.87	6.57	0.92	11.98	6.57	0.67	6.56
(10,0) SWCNT/GNR	2.29	1.21	0.97	4.61	8.38	10.53	8.28
(11,0) SWCNT/GNR	2.50	1.21	1.04	6.70	9.45	4.64	6.89
(13,0) SWCNT/GNR	2.69	1.22	1.24	2.89	9.03	22.33	9.00
(14,0) SWCNT/GNR	2.07	1.05	1.28	4.05	10.20	20.67	7.09
(16,0) SWCNT/GNR	2.61	1.64	1.32	2.60	8.04	36.98	9.77
SWCNT							
(8,0) SWCNT	4.38	6.91	0.42	7.25	3.89	0.69	1.21
(10,0) SWCNT	2.69	2.66	0.55	5.49	5.50	3.25	3.31
(11,0) SWCNT	6.83	4.56	0.60	6.20	6.27	0.70	1.25
(13,0) SWCNT	2.29	2.69	0.70	5.52	5.57	5.28	4.07
(14,0) SWCNT	5.04	3.58	0.77	6.18	6.12	1.42	2.42
(16,0) SWCNT	1.90	2.28	0.89	5.59	5.64	8.68	6.47
GNR	2.67	1.32	0.44	5.61	7.08	2.52	4.56

3.2. The effect of SWCNT diameter on the mobility of charge carriers in hybrid structures of SWCNTs/GNRs

Figure 2 shows the Mulliken distributions of the electron charge density on the supercell atoms of the SWCNT/GNR hybrid structures. As can be seen from the figure, the largest charge is localized in the octagonal junction region, with a region of excess positive charge forming on the GNR (shown in red in the figure), and on SWCNT — a region of negative charge (shown in blue in the figure). Also of note are the 2 edge layers of carbon atoms along the „chair“

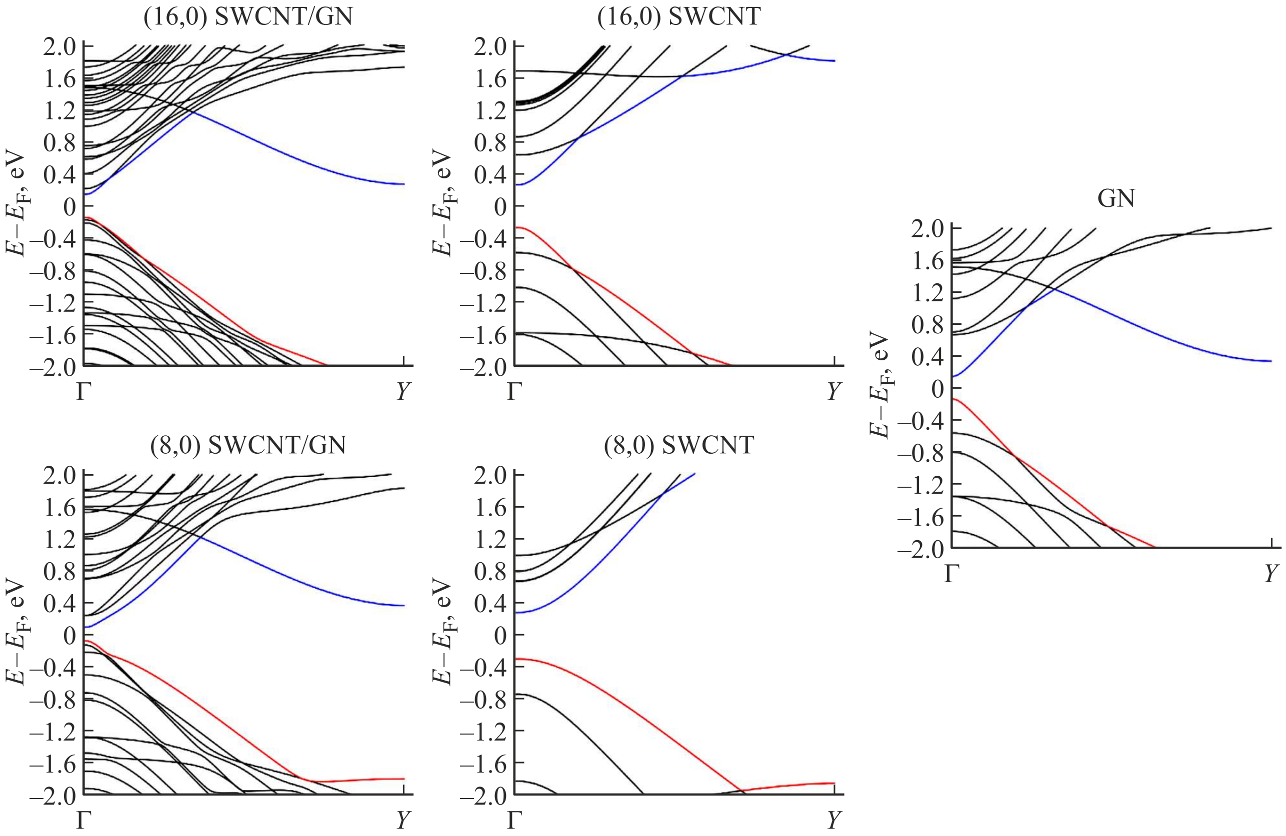

Figure 3. Fragments of band structures near the Fermi E_F level (shifted in the plots to 0 eV) for supercells of SWCNTs (8.0)/GNR and SWCNTs (16.0)/GNR, as well as their constituent SWCNTs and GNR. The bottom of the conduction band is shown in blue, and the top of the valence band is shown in red. Point Y corresponds to the boundary of the first Brillouin zone.

direction of the hexagonal lattice GNR. The atoms at the top of the GNR tip (yellow-green in the figure) acquire a total charge of 0.05 e. The atoms in the neighboring layer (bright green in the figure) acquire a total charge of −0.06 e. All other atoms of the supercells remain electrically neutral.

Let us determine the logic behind the formation of the band structure of SWCNT/GNR hybrids on the example of SWCNT(8.0)/GNR and SWCNT(16.0)/GNR supercells. Fragments of the band structures near the Fermi level (shifted in the plots to 0 eV) for the above supercells of SWCNT/GNR, as well as for the SWCNT and GNR included in them, are shown in Figure 3. As can be seen from the figure, the energy profile of the valence band and conduction band of the hybrid SWCNT/GNR structures is formed from fragments of the energy profiles of their constituent SWCNT and GNR. In particular, it can be noted that the parabolic subband, which is the bottom of the conduction band in the band structure of GNR (highlighted in blue in the figure), is present at the same place in the band structure of SWCNT/GNR. The appearance of this subzone leads to a noticeable reduction in the forbidden zone width E_g of hybrid SWCNT/GNR structures compared to the values of individual SWCNT. For example, the E_g value for the (16,0)/GNRs hybrid structure is 0.28 eV, while for the (16,0) and GNRs — 0.53 and 0.28 eV, respectively. The E_g value for the (8,0)/GNR hybrid structure is 0.17 eV, whereas for the individual SWCNT (8,0) and GNR — 0.58 and 0.28 eV, respectively. A similar trend was observed for SWCNT/GNR supercells with other nanotubes: the discrepancy in E_g values between SWCNT/GNR and individual GNR is 0.04 eV on average. Thus, we can say that the E_g value of the hybrid SWCNT/GNR structures tends to the E_g value of the GNR included into them. We can also note the similarity in the values of the derivative (slope angle near the point Γ) of the energy of the subband, which is the top of the valence band, of SWCNTs/GNRs and nanotubes included into them. The noted logic will be further manifested in the calculated values of the effective mass of charge carriers in the hybrid structures of SWCNT/GNR and their components.

The effective mass of charge carriers (electrons m_e^* and holes m_h^*) in hybrid SWCNT/GNR structures and their constituent SWCNTs and GNRs was calculated using the values of the conduction band bottom energy and the valence band top. The calculation results are shown in Table 1, from which it follows that the effective mass of charge carriers in the hybrid structures is not strictly correlated with the tube diameter and averages 2.67 $[0.01m_0]$ for electrons and 2.15 $[0.01m_0]$ for holes. At the same time, for SWCNTs that are part of supercell SWCNT/GNR

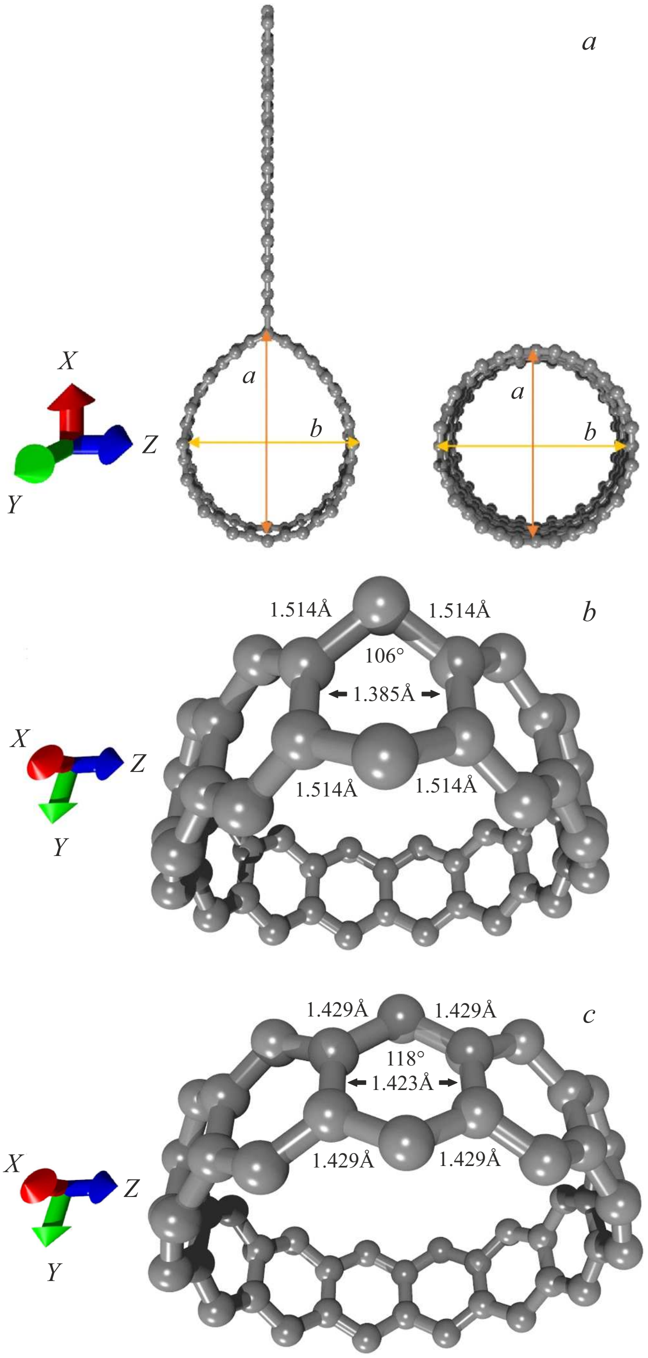

Figure 4. *a* — of the SWCNT (13,0) supercell and the SWCNT (13,0)/GNR hybrid structure with parameter designation a/b, where a — size of the supercell along the X axis, b — along the Z axis; b — supercell of the SWCNT (13,0), which is in the hybrid SWCNT (13,0)/HN structure, and the common SWCNT (13,0).

structures, the effective mass of electrons is 3.86 $[0.01m_0]$, and that of holes is m_h^* — 3.78 $[0.01m_0]$. It should also be noted that both the effective mass of electrons m_e^*, and the effective mass of holes m_h^* of SWCNTs change in a stepwise manner as nanotube diameter increases, with $(n, 0$ for SWCNTs), where $n = 3q + 1$ $(q = 2{-}5)$ $m_e^* > m_h^*$, and $(n, 0$ for SWCNTs), where $n = 3q + 2$ $(q = 2m_e^* < m_h^*)$.

The observed logic behind the changes in the effective masses of charge carriers in SWCNTs of the „zigzag" type agrees well with the results of numerical studies obtained earlier by other authors also as part of the deformation potential theory of Bardeen and Shockley [27,28]. At the same time, in terms of m_e^* and m_h^* values of SWCNT $(n, 0)$ there are differences between all three papers — ours, [27] and [28]. Let us illustrate them using the example of SWCNT (13,0): $m_e^* = 6.91$ $[0.01m_0]$, $m_h^* = 6.89$ $[0.01m_0]$ in [27], $m_e^* = 25$ $[0.01m_0]$, $m_h^* = 25$ $[0.01m_0]$ in [28], $m_e^* = 2.29$ $[0.01m_0]$, $m_h^* = 2.69$ $[0.01m_0]$ in our study. The differences in the values can be explained as follows. First, despite the identical chirality indices of the „zigzag" type SWCNT in all three papers, the atomic structures of the nanotubes have major differences. In [27], nanotubes containing point defects of the Stone–Wales type and of the 5-8-5 type with different concentrations were considered, while [28] studied defect-free nanotubes, but its authors did not provide any data either on the translation vectors of the calculated supracells or on what each cell was and how many atoms were included in its composition. Furthermore, in [27,28] it was assumed that the nanotubes had a perfect cylindrical shape. In our study, the calculations were performed for geometric models of nanotubes „cut out" from the supercells of hybrid SWCNT/GNR structures. As mentioned earlier in section 3.1, the nanotubes were highly deformed during the formation of covalent bonding with the GNRs. In particular, if we introduce the parameter a/b, which is the ratio of the maximum dimensions for the supercells of the tubes along the X and Z axes, as shown in Figure 4, *a* for the example of SWCNT (13,0), then for all SWCNT fragments included in the supercells of the SWCNT/GNR hybrid structures, it is 1.25, whereas it is $a/b = 1$ for nanotubes of ideal cylindrical shape. The lengths of C–C-bonds between atoms within hexagons are also different for SWCNTs cut from supercells of hybrid structures and for SWCNTs not originally part of the composite object. Figure 4, *b* shows these differences using the example of a SWCNT hexagon whose atoms form covalent bonds with graphene as part of a SWCNT/GNR hybrid. In addition to the difference in the lengths of C–C-bonds, this figure also shows the difference in the values of valence angles between C–C-bonds at the top of the hexagon under consideration: 106° for SWCNTs in the SWCNT/GNR hybrid, 118° for a regular SWCNT. It is well known that the electron-energy characteristics of nanotubes, including the band diagrams, are extremely sensitive to changes in their geometrical parameters. Consequently, the energy values determined based on the band diagrams will also be largely determined by the geometrical parameters of the calculated supercells. Secondly, the calculations of nanostructure band diagrams are sensitive to the accuracy of the partitioning of the first Brillouin band, determined by the number of points used in k-space, and to the choice of basis sets and

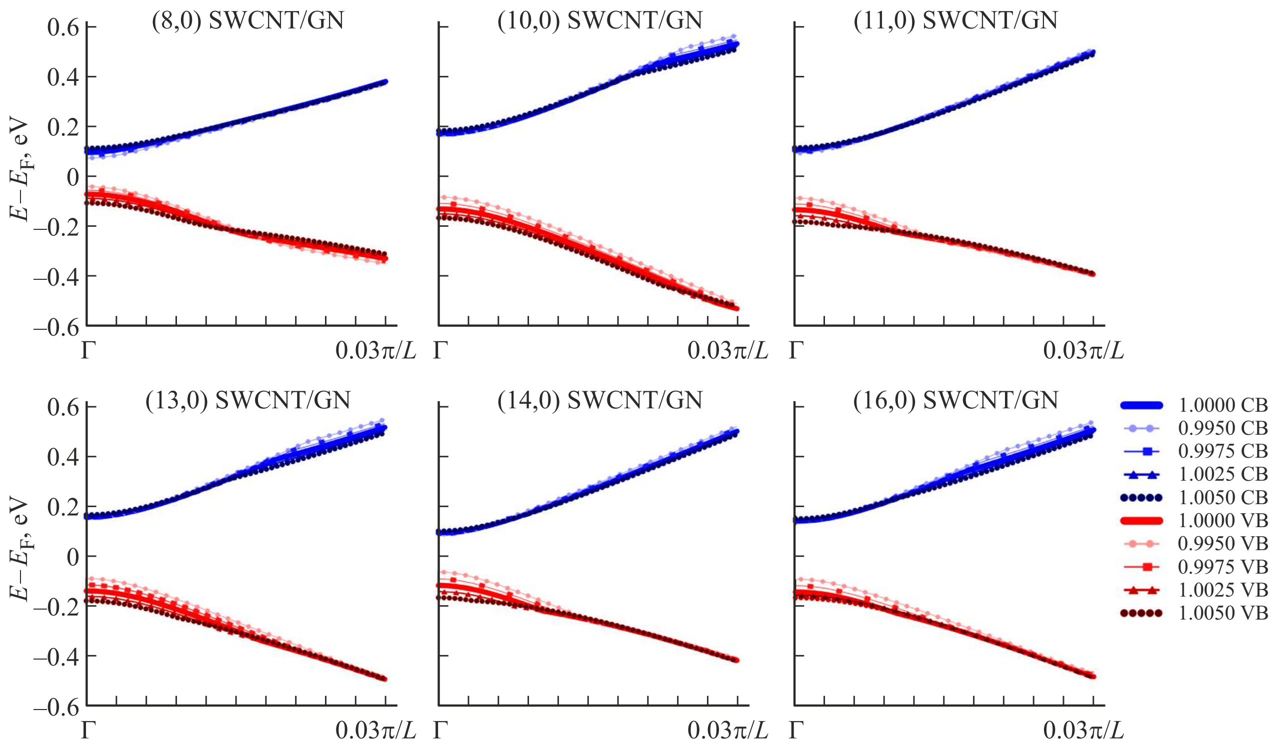

Figure 5. Energy diagrams near the valence band top (shades of red) and conduction band bottom (shades of blue) for deformed supercells of SWCNT/GNR hybrid structures with different SWCNT chirality. The band structure is shown in the interval from point Γ to $0.03\,\pi/L$ (L — translation vector along the tube). (A color version of the figure is provided in the online version of the paper).

functionals used as part of the DFT theory and determining the accuracy of the calculations. In particular, the hybrid empirical B3LYP functional was used in [27], while we and the authors of [28] used the more recent non-empirical GGA correlation functional PBE. The PBE functional provides good agreement between the calculated and experimental data on the electronic structure of carbon nanotubes [29] and is widely used to calculate the band diagrams of carbon nanostructures [30–33]. The sets of basis functions used also differed: in [27] we used Gaussian functions with the addition of polarization functions 6-21G(d), in [28] — plane wave bases, and we used Slater functions with the addition of a double set of polarization functions DZP „zeta“. The partitioning of the first Brillouin zone in [27] was rather coarse and was carried out using only 41 hboxin k-space, in [28] 150 points were used, we used 200 points. Thus, our calculations of the atomic structure of supercells and band diagrams are characterized by the highest accuracy compared with [27,28].

In accordance with the algorithm of carrier mobility calculation described above (Section 2. Research Methods), the supercells of SWCNT/GNR hybrid structures were compressed and stretched along the translation direction (along the Y axis). The results of calculating the value of C_{1D}^{β} are given in Table 1. As can be seen, an increase in C_{1D}^{β} is observed when the nanotube diameter increases. This leads to a decrease in the deformation potential, i. e., a decrease in the influence of acoustic waves, which prevent the passage of charge carriers in hybrid SWCNT/GNR structures. It can be assumed that the mobility of carriers in hybrid SWCNT/GNR structures will increase with increasing SWCNT diameter, which will be shown further.

Further, for the deformed supercells of SWCNT/GNR hybrid structures, the zone structure was calculated, and the bottom of the conduction band (for calculating the deformation potential of electrons) and the top of the valence band (for calculating the deformation potential of the holes) were determined from a fragment of it near the Fermi level. The calculated energy diagrams near the Fermi level are shown in Figure 5. It can be seen from the figure that the SWCNT/GNR hybrid structures with nanotubes (8.0), (11.0), and (14.0) are characterized by a more obvious deformation of the energy subbands near the bottom of the conduction band and near the valence band ceiling compared to the SWCNT/GNR hybrid structures with nanotubes (10.0), (13.0), and (16.0). Thus, upon deformation of SWCNT/GNR hybrid structures with nanotubes (8.0), (11.0), and (14.0), the energy subzones are separated from each other by a larger interval. The observed differences are due to the fact that the phenomenon of aromaticity, the idea of which is that the orbitals of neighboring atoms in carbon rings form a common electron cloud, occurs at chirality indices SWCNT, varying with a certain periodicity [34,35]. The presence of a common electron cloud increases the bonding strength between

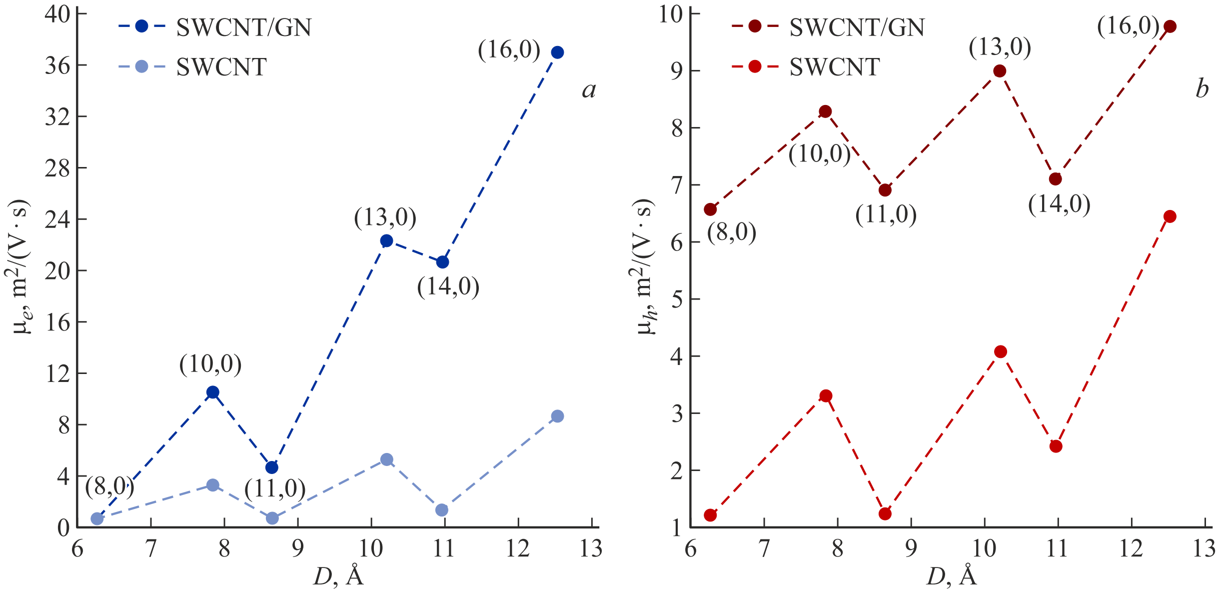

Figure 6. Plots of the dependence of electron (*a*) and (*b*) hole mobility in SWCNT/GNR and SWCNT hybrid structures on the SWCNT diameter.

neighboring atoms and, consequently, decreases the deformation potential. The results of deformation potential calculation are summarized in Table 1. It can be noted that the deformation potential of SWCNT/GNR hybrid structures with SWCNT (8.0), (11.0) and (14.0) is higher compared to that of SWCNT/GNR hybrid structures with SWCNT (10.0), (13.0) and (16.0). As the SWCNT diameter increases, the deformation potential for electrons decreases from 11.98 to 2.60 eV, while the deformation potential for holes has no strict dependence on the SWCNT diameter. The average value of the deformation potential for the holes (8.61 eV) is higher than that for the electrons (5.47 eV). In case of individual SWCNTs, the opposite pattern is observed: the average value of the deformation potential for holes and electrons is 5.50 and 6.04 eV, respectively. This is due to the influence that GNR has on the deformation potential of SWCNT/GNR hybrid structures. For GNR, the deformation potential is 7.08 and 2.99 eV for holes and electrons, respectively.

Once the magnitude of the charge carrier deformation potential was obtained, the electron and hole mobility in SWCNT/GNR hybrid structures was calculated. To compare, the charge carrier mobility was also calculated separately for SWCNTs and GNRs, which are included in the supercells of SWCNT/GNR hybrid structures. The diagrams illustrating the dependence of charge carrier mobility on SWCNT diameter are shown in Figure 6. As one can see from the figure, the mobility change has an oscillating character both for SWCNT/GNR hybrids and for nanotubes included in their composition, which indicates a significant contribution of nanotubes to the electrophysical properties of graphene-nanotube 1*D*-structures. In case of the nanotubes included with the SWCNT/GNR hybrid, it can also be noted that for SWCNT $(n, 0)$, where $n = 3q + 1$ $(q = 2{-}5)$ $\mu_e^* > \mu_h^*$ and for SWCNT $(n, 0)$, where $n = 3q + 2$ $(q = 2{-}5)$ $\mu_e^* < \mu_h^*$, which qualitatively agrees well with the results provided in [27,28]. he quantitative differences in the mobility values of μ_e^* and μ_h^* with the results of [27,28] are due to the same reasons as the differences in the effective masses of m_e^* and m_h^* described above. The observed oscillations of mobility values can be explained by the property of aromaticity of carbon rings [34,35]. The average electron mobility $(15.97\,\mathrm{m^2/(V \cdot s)})$ in SWCNT/GNR hybrids is higher than the average hole mobility $(7.93\,\mathrm{m^2/(V \cdot s)})$ due to the higher value of the deformation potential for holes compared to electrons. The electron and hole mobilities of the individual GNR are 2.52 and $4.56\,\mathrm{m^2/(V \cdot s)}$ respectively. In general, it can be noted that the synergistic effect caused by the combination of SWCNTs and GNRs leads to a several-fold increase in the mobility of charge carriers in SWCNT/GNR hybrid structures compared to individual graphene and nanotube. The (16.0) SWCNT /GNR hybrid structure is characterized by the highest charge carrier mobility.

3.3. The effect of GNR width on the mobility of charge carriers in SWCNT/GNR hybrid structures SWCNT/GNR

In the previous step of the study, we have shown that the highest charge carrier mobility in the SWCNT/GNR hybrid structure is achieved at SWCNT (16,0). The next step was to establish the nature of the influence of topological features of GNRs on the carrier mobility in SWCNT/GNR hybrid structures. We built 6 supercells of (16,0) SWCNT/GNR hybrid structures with GNR widths

Table 2. The elasticity constant C_{1D}^{β}, the effective mass of electrons m_e^* and holes m_h^* (in units of electron mass m_0), and the deformation potential of electrons E_e^{β} and holes E_h^{β} of the (16,0) SWCNT GNR hybrid structure with varying width GNR

Band width, Å	m_e^*, $0.01m_0$	m_h^*, $0.01m_0$	$C_{1D}^{\beta} \cdot 10^{11}$, eV/cm	E_e^{β}, eV	E_h^{β}, eV	μ_e^*, $m^2/(V \cdot s)$	μ_h^*, $m^2/(V \cdot s)$
9.81	4.75	4.47	1.15	3.11	2.13	9.12	21.15
12.26	4.25	4.53	1.10	2.97	2.12	11.24	20.17
14.70	2.85	4.20	1.15	3.13	4.43	19.26	5.41
17.16	2.16	2.38	1.20	3.66	5.69	22.50	8.02
19.16	4.33	5.42	1.33	2.09	3.23	26.88	8.06
22.17	2.61	1.64	1.32	2.60	8.04	36.98	7.77

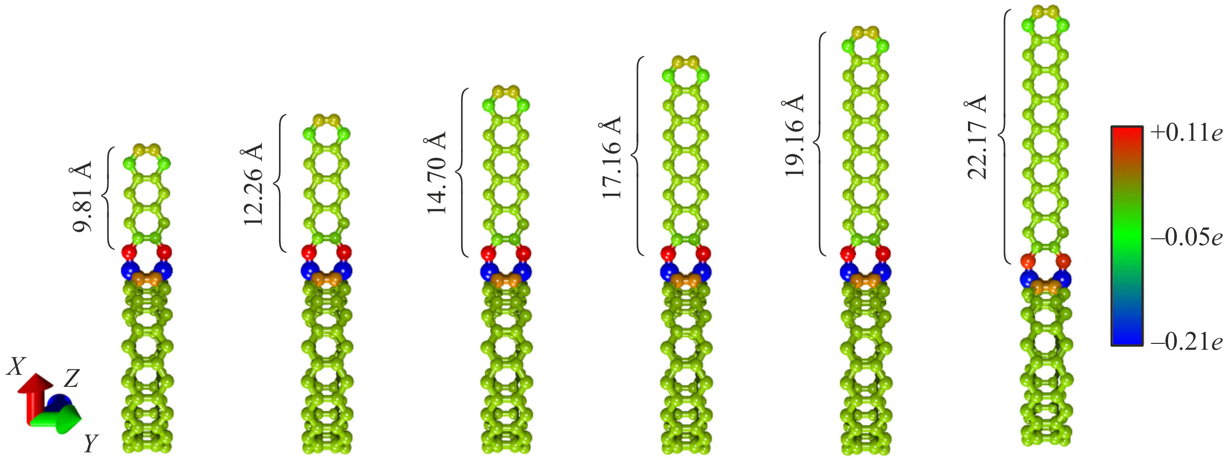

Figure 7. Mulliken electron charge density distribution over the supercell atoms of hybrid structures (16,0) SWCNT/GNR with nanoribbons of varying widths.

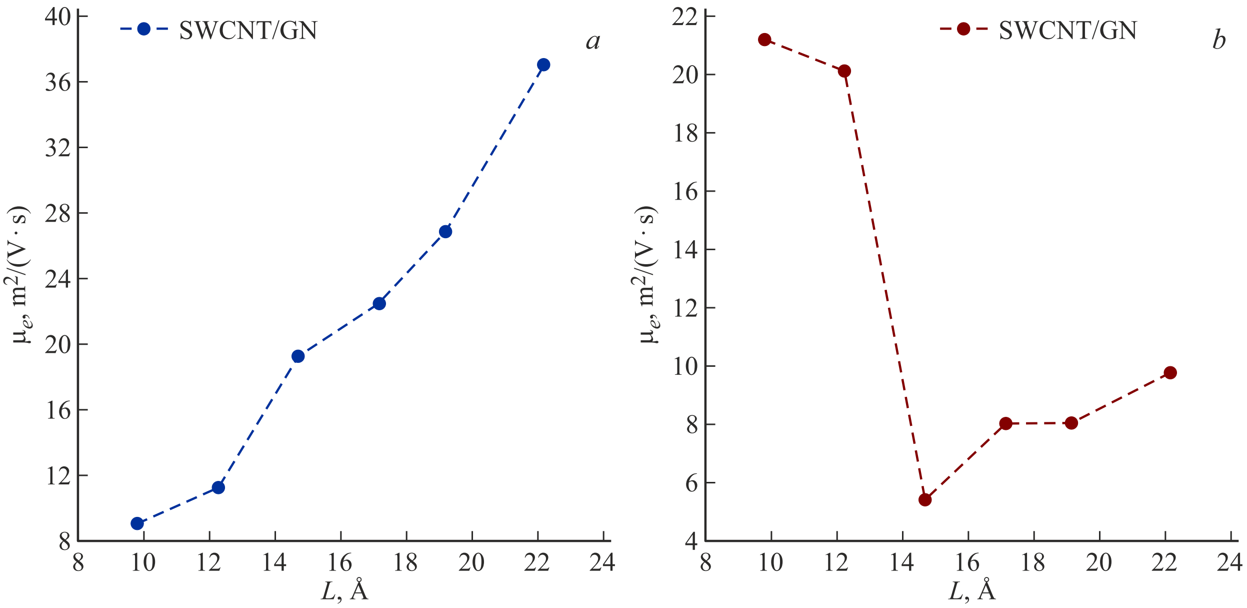

Figure 8. The mobility of (*a*) electrons and (*b*) holes in SWCNT/GNR and SWCNT hybrid structures as a function of band width.

varying from 9.81 to 22.1 Å, and found their equilibrium configurations. The Mulliken electron charge density distributions of the atoms of the constructed supercells of the (16,0) SWCNT/GNR hybrid structures are shown in Figure 7. The analysis of the obtained calculation results shows that the width of GNR does not affect the character of partial charge distribution in SWCNT/GNR hybrid structures.

The calculated values of the elasticity constant, effective mass and deformation potential for supercells of SWCNT (16,0)/GNR hybrid structures are summarized in Table 2. It follows from the table that the width of the GNR has no significant effect on the values of the effective mass of charge carriers in SWCNT/GNR hybrid structures. The average values of the effective masses of holes and electrons are 3.49 $[0.01m_0]$ and 4.05 $[0.01m_0]$ respectively, which is almost 2 times higher than those of the SWCNT/GNR hybrid structures as the diameter of SWCNTs increases (see Table 1). The increase in GNR width leads to an increase in the elasticity constant from $1.15 \cdot 10^{11}$ to $1.32 \cdot 10^{11}$ eV/cm, a decrease in the deformation potential for electrons from 3.11 to 2.60 eV and its increase for holes from 2.13 to 8.04 eV.

The results of carrier mobility calculation in (16,0) SWCNT/GNR hybrid structures with varying nanoribbon width are shown in Figure 8. It can be seen from the figure that as the GNR width increases, the electron mobility increases almost according to a linear law in the range from 9.12 to $36.98\,\mathrm{m^2/(V \cdot s)}$. At the same time, the hole mobility changes non-monotonically: a sharp decline to the value of $5.41\,\mathrm{m^2/(V \cdot s)}$ with a width of GNR 14.70 Å is replaced by a fairly smooth growth at a GNR width in the range 14.70–22.17 Å. The maximum hole mobility of 21.15 and $20.17\,\mathrm{m^2/(V \cdot s)}$ is observed at GNR widths of 9.81 and 12.26 Å, respectively.

The high hole mobility at small GNR width is explained by the previously established patterns of charge distribution in the (16,0) SWCNT/GNR hybrid structure (Figure 6). As one can see from Figure 6, the atoms of the seamless octagonal SWCNT and GNR connection localize the excess positive charge domain. As the GNR width decreases, this domain shifts closer to the vacuum layer (at the edge of GNR), in which acoustic waves cannot propagate, preventing the propagation of holes.

4. Conclusion

The following logic has been discovered as part of a DFT study using the Bardeen–Shockley theory to calculate the charge carrier mobility in hybrid SWCNT/GNRs:

1) the elasticity constant for the hybrid SWCNT/GNR structures increases as the diameter of SWCNT/GNR increases (from 6.264 to 12.529 Å) by 1.43 times (from 0.92 to 1.32 eV/cm) and by 1.15 times (from 9.81 to 22.17 Å) when the ribbon GNR width increases (from 1.15 to 1.32 eV/cm);

2) increasing the diameter of SWCNT, which is part of the SWCNT/GNR hybrid structure, by 2 times (from 6.264 to 12.529 Å), increases electron mobility by ~ 55 times (from 0.67 to $36.98\,\mathrm{m^2/(V \cdot s)}$) and hole mobility by ~ 1.5 times (from 6.56 to $9.77\,\mathrm{m^2/(V \cdot s)}$);

3) increasing the GNR band width by ~ 2.26 times (from 9.81 to 22.17 Å) increases the electron mobility by ~ 4 times (from 9.12 to $36.98\,\mathrm{m^2/(V \cdot s)}$) and decreases the hole mobility by ~ 2.7 times (from 21.15 to $7.77\,\mathrm{m^2/(V \cdot s)}$).

The observed difference in mobility behavior for electrons and for holes is explained by higher values of the deformation potential for holes compared to electrons.

Thus, SWCNTs of larger diameter should be used to increase the mobility of charge carriers of both signs within SWCNT/GNR hybrid structures. Varying the width of GNRs in SWCNT/GNR hybrid structures affects the mobility of charge carriers in them in a different way: the mobility of electrons increases as the width of GNRs increases, while the mobility of holes decreases. Among the topological variants of hybrid graphene-nanotube $1D$-structures considered in this study, the (16,0) SWCNT/GNR configuration with a GNR width of 22.17 Å showed the highest mobility of carriers of both signs.

Funding

The study was financially supported by the state assignment of the Ministry of Education and Science FSRR-2023-0008.

Conflict of interest

The authors declare that they have no conflict of interest.

References

[1] S. Rathinavel, K. Priyadharshini, D. Panda. Mater. Sci. Eng. B, **268**, 115095 (2021).

[2] Q. Ji, B. Wang, Y. Zheng, X. Yan, F. Zeng, B. Lu. J. Alloys Compd., **897**, 163136 (2022).

[3] P.N.D. Duoc, N.H. Binh, T. Van Hau, C.T. Thanh, P. Van Trinh, N.V. Tuyen, N. Van Quynh, N. Van Tu, V.D. Chinh, V.T. Thu, P.D. Thang, P.N. Minh, N. Van Chuc, J. Hazard. Mater., **400**, 123185 (2020).

[4] X. Zhang, X. Zhang, Y. Zhang, Y. Liu, W. Peng. IEEE Trans. Instrum. Meas., **70**, 1 (2021).

[5] Ö. Güler, Ç. Yavuz, Ö. Başgöz, S. Altın, I.S. Yahia. J. Mater. Sci.: Mater. Electron., **31**, 3184 (2020).

[6] Y. Zhong, K. Deng, J. Zheng, T. Zhang, P. Liu, X. Lv, W.J. Ji. J. Mater. Sci. Technol., **149**, 205 (2023).

[7] Q. Ji, B. Wang, Y. Zheng, F. Zeng, B. Lu. Diamond. Relat. Mater., **124**, 108940 (2022).

[8] J.S. Han, S.H. Lee, H. Go, S.J. Kim, J.H. Noh, C.J. Lee. ACS Nano, **16** (7), 10231 (2022).

[9] H.R. Lee, O.J. Hwang, B. Cho, K.C. Park. Vacuum, **182**, 109696 (2020).

[10] T. Kim, S. Fan, S. Lee, M.K. Joo, Y.H. Lee. Sci. Rep., **10** (1), 13101 (2020).

[11] Darabi, M.R. Salehi, E. Abiri. ECS J. Solid State Sci. Technol., **11** (3), 031007 (2022).
[12] X. Hong, W. Shi, H. Zheng, D. Liang. Vacuum, **169**, 108917 (2019).
[13] M.N. Dang, M.D. Nguyen, N.K. Hiep, P.N. Hong, I.H. Baek, N.T. Hong. Nanomaterials, **10** (10), 1931 (2020).
[14] J.Y. Oh, G. H. Jun, S. Jin, H. J. Ryu, S. H. Hong. ACS Appl. Mater. Interfaces, **8** (5), 3319 (2016).
[15] M.N. Barshutina, V.S. Volkov, A.V. Arsenin, D.I. Yakubovsky, A.V. Melezhik, A.N. Blokhin, A.G. Tkachev, A.V. Lopachev, V.A. Kondrashov. Nanomaterials, **11** (5), 1143 (2021).
[16] J. Foroughi, G.M. Spinks, D. Antiohos, A. Mirabedini, S. Gambhir, G.G. Wallace, S.R. Ghorbani, G. Peleckis, M.E. Kozlov, M.D. Lima, R.H. Baughman. Adv. Funct. Mater., **24** (37), 5859 (2014).
[17] M. Chen, L. Zhang, S. Duan, S. Jing, H. Jiang, C. Li. Adv. Funct. Mater., **24** (47), 7548 (2014).
[18] D.D. Nguyen, N.H. Tai, S.Y. Chen, Y.L. Chueh. Nanoscale, **4** (2), 632 (2012).
[19] W.J. Yu, S.Y. Lee, S.H. Chae, D. Perello, G.H. Han, M. Yun, Y.H. Lee. Nano Lett., **11** (3), 1344 (2011)
[20] V.V. Ivanovskaya, A. Zobelli, P. Wagner, M.I. Heggie, P.R. Briddon, M.J. Rayson, C.P. Ewels. Phys. Rev. Lett., **107** (6), 065502 (2011).
[21] M.A. Akhukov, S. Yuan, A. Fasolino, M.I. Katsnelson. New J. Phys., **14** (12), 123012 (2012).
[22] The SIESTA group [Electronic source]. Available at: departments.icmab.es/leem/siesta/ (date of access: 03.07.2024). Cover from screen. Lang. — EN.
[23] A. García, N. Papior, A. Akhtar, E. Artacho, V. Blum, E. Bosoni, P. Brandimarte, M. Brandbyge, J.I. Cerdá, F. Corsetti, R. Cuadrado, V. Dikan, J. Ferrer, J. Gale, P. García-Fernández, V.M. García-Suárez, S. García, G. Huhs, S. Illera, R. Korytár, P. Koval, I. Lebedeva, L. Lin, P. López-Tarifa, S.G. Mayo; S. Mohr, P. Ordejón, A. Postnikov, Y. Pouillon, M. Pruneda, R. Robles, D. Sánchez-Portal, J.M. Soler, R. Ullah, V. Wen-zhe Yu, J. Junquera. J. Chem. Phys., **152** (20), 204108 (2020).
[24] J. Xi, M. Long, L. Tang, D. Wang, Z. Shuai. Nanoscale, **4** (15), 4348 (2012).
[25] J. Bardeen, W.J.P.R. Shockley. Phys. Rev., **80** (1), 72 (1950).
[26] A. Yamanaka, S. Okada. Carbon, **96**, 351 (2016).
[27] H. Bai, H. Gao, Y. Ma, Q. Wang, Y. Wu. Diamond Relat. Mater., **109**, 108013 (2020).
[28] B. Xu, Y.D. Xia, J. Yin, X.G. Wan, K. Jiang, A.D. Li, D. Wu, Z.G. Liu. Appl. Phys. Lett., **96**, 183108 (2010).
[29] G. Dresselhaus, M.S. Dresselhaus, R. Saito. *Physical properties of carbon nanotubes* (Singapore, World Scientific, 1998).
[30] S. Castan, G. Sigmund, T. Hüffer, N. Tepe, F. von Der Kammer, B. Chefetz, T. Hofmann. Environ. Sci.: Process. Impacts, **22** (9), 1888 (2020).
[31] P.V. Avramov, K.N. Kudin, G.E. Scuseria. Chem. Phys. Lett., **370**, 597 (2003). DOI: 10.1016/S0009-2614(03)00113-1
[32] E.Y. Li. Carbon, **100**, 187 (2016). DOI: 10.1016/j.carbon.2015.12.083
[33] F. Buonocore, A. Capasso, M. Celino, N. Lisi, O. Pulci. J. Phys. Chem. C, **125**, 16316 (2021). DOI: 10.1021/acs.jpcc.1c04397
[34] S.M. Monavari, F. Marsusi, N. Memarian, M. Qasemnazhand. Sci Rep., **13**, 3118 (2023). DOI: 10.1038/s41598-023-29862-9
[35] H.M. Yu, S. Sharma, S. Agarwal, O. Liebmana, A.S. Banerjee. RSC Adv., **14**, 963 (2024). DOI: 10.1039/D3RA06988E

Translated by J.Savelyeva